William F. Sherman[1]
Center for Complex Biological Systems,
Edwards Lifesciences Center for Advanced Cardiovascular Technology,
University of California,
Irvine, CA 92697
e-mail: wsherma1@uci.edu

Mira Asad
Edwards Lifesciences Center for Advanced Cardiovascular Technology,
Department of Biomedical Engineering,
University of California,
Irvine, CA 92697
e-mail: mnasad@uci.edu

Anna Grosberg[1]
Edwards Lifesciences Center for Advanced Cardiovascular Technology,
Department of Biomedical Engineering,
NSF-Simons Center for Multiscale Cell Fate Research,
University of California,
Irvine, CA 92697;
Department of Chemical and Biomolecular Engineering,
Center for Complex Biological Systems,
University of California,
Irvine, CA 92697
e-mail: grosberg@uci.edu

An Energetic Approach to Modeling Cytoskeletal Architecture in Maturing Cardiomyocytes

Through a variety of mechanisms, a healthy heart is able to regulate its structure and dynamics across multiple length scales. Disruption of these mechanisms can have a cascading effect, resulting in severe structural and/or functional changes that permeate across different length scales. Due to this hierarchical structure, there is interest in understanding how the components at the various scales coordinate and influence each other. However, much is unknown regarding how myofibril bundles are organized within a densely packed cell and the influence of the subcellular components on the architecture that is formed. To elucidate potential factors influencing cytoskeletal development, we proposed a computational model that integrated interactions at both the cellular and subcellular scale to predict the location of individual myofibril bundles that contributed to the formation of an energetically favorable cytoskeletal network. Our model was tested and validated using experimental metrics derived from analyzing single-cell cardiomyocytes. We demonstrated that our model-generated networks were capable of reproducing the variation observed in experimental cells at different length scales as a result of the stochasticity inherent in the different interactions between the various cellular components. Additionally, we showed that incorporating length-scale parameters resulted in physical constraints that directed cytoskeletal architecture toward a structurally consistent motif. Understanding the mechanisms guiding the formation and organization of the cytoskeleton in individual cardiomyocytes can aid tissue engineers toward developing functional cardiac tissue. [DOI: 10.1115/1.4052112]

1 Introduction

A healthy heart is able to regulate its complex dynamics due to its organized, hierarchical structure [1,2]. In diseased hearts, this high degree of organization is inhibited with many physiological and structural properties appearing compromised [3–5]. For instance, cardiomyocytes from diseased hearts exhibit changes in cell size and shape [6]. In isolated cardiomyocytes, cell shape changes have been associated with inhibited cell contractility and reduced sarcomeric registration [7]. To study whether there is a link between the altered cellular structure and the inhibited function of cardiomyocytes, engineered tissue capable of recapitulating the phenomenological properties found in maladaptive cardiac tissue must be developed. One such property is the organization of the cytoskeleton at different length scales. For example, cardiac tissue may be globally isotopic while being locally anisotropic [8]. Controlling this balance in organization at the global and local scales is an ongoing challenge. Spatial constraints further complicate matters as myofibrils are multidimensional constructs and need to compete for space in a densely packed environment [9]. As a result, individual cells may contain myofibrils with vastly different lengths, curvatures, and locations, in some cases even having their placement impacted by the presence of the nucleus [10]. Each of these factors contributes to the challenge of mimicking cytoskeletal organization in engineered tissue. The development of computational models capable of recapitulating these observed behaviors may serve as an invaluable tool. Modeling provides a means for efficiently exploring these characteristics and may lead to better control of the cytoskeletal architecture in vitro.

Numerous theoretical models have been employed to address how cytoskeletal organization might be obtained, as has been recently reviewed [11]. Kassianidoua et al. explored how the cytoskeletal architecture was related to stress fiber mechanics using a minimalistic active cable network model [12]. They considered how stress fiber connections could influence individual stress fiber mechanics. However, the model did not address the influence of cell geometry on fiber shape and only considered a small, simplified portion of the cytoskeletal network. Yuan et al. Produced a model that allowed for the geometry of the cell to be included and predicted the mechanical stress in the cytoskeleton [13]. By including the dynamics of focal adhesions, the collection of proteins that anchor the cell to the substrate, they were able to predict the myofibril-associated principle stress direction in both regular and irregularly shaped cells. This model did not consider spatial constraints that would cause a myofibril to interact with neighboring myofibrils or other internal organelles like the nucleus. It also did not provide a prediction of where the myofibrils would be located within the cell. Several other models have followed suit, considering the interaction between focal adhesion dynamics and resulting traction stress measurements but not addressing myofibril placement [14–16]. Consequently, previous models have been unable to recapitulate the internal architecture observed experimentally [17,18].

In this work, we utilized the myofibril force-focal adhesion relation [19] to simulate the interplay between focal adhesion dynamics and cytoskeleton construction simultaneously, allowing the development of a dynamically changing cytoskeletal network. Our model considered how a cell attached to a flat ECM island of a particular geometry might lead to alterations in the cytoskeleton, allowing us to explore the impact of cellular boundary cues on intracellular architecture. By controlling cell size and shape as well as nucleus size and location, we were able to generate myofibril networks that could vary depending on several stochastic

[1]Corresponding authors.

Manuscript received March 7, 2021; final manuscript received July 28, 2021; published online September 21, 2021. Assoc. Editor: Nicole Hashemi.

factors. While these factors may influence the cell's cytoskeletal architecture, our approach provides useful information regarding the formation of any given cytoskeleton by linking myofibril maturation, the number of myofibril bundles present in the network, and the ability to adapt to a changing focal adhesion distribution.

2 Materials and Methods

2.1 Integrin Based Focal Adhesion Model. The focal adhesion model was based on a simplified classification of the density of integrin proteins into either a bound or unbound state, denoted ρ_b and ρ^*, respectively. Following kinematic modeling approaches, it was assumed that there was a competition between the integrin-binding and unbinding rates. Since there have been many experimental observations regarding the binding and growth rate of focal adhesion proteins increasing with force magnitude [19,20], the binding rate of unbound integrins was assumed to increase linearly with force magnitude, $k_0 + k_1|\mathbf{F}|$. Here, $|\mathbf{F}|$ denotes the net force applied to the focal adhesion at $\mathbf{x}$. As more integrins begin to bind within a region, the developing focal adhesion was expected to become stabilized and less likely to disassemble [21]. As such, the unbinding rate was expected to be smaller than the binding rate for large force magnitude values. On the other hand, to allow for rapid disassembly of initial focal adhesion complexes that may form sporadically due to randomized initial density distribution, the unbinding rate was assumed to be larger than the binding rate for smaller force magnitude values. This behavior was captured using an unbinding rate of the form $k_{-1}\exp(|\mathbf{F}|/F_0)$. This gave the kinetic equation for the density of bound integrins:

$$\frac{\partial \rho_b}{\partial t} = (k_0 + k_1|\mathbf{F}|)\rho^* - k_{-1}e^{|\mathbf{F}|/F_0}\rho_b \tag{1}$$

The density of free integrins was derived by assuming that unbound integrins can diffuse throughout the 2-D cell at a much faster rate than all other processes in the cell [13,14]. Under this simplifying assumption, the density of free integrins was derived by considering the difference in the average integrin density in the cell, $\bar{\rho}$, and the density of bound integrins. This yielded

$$\rho^* = \frac{1}{A}\int_\Psi (\bar{\rho} - \rho_b)d^2\mathbf{x}' \tag{2}$$

where Ψ defines the cell geometry having area A.

2.2 Integrin-Cytoskeleton Based Force Model. It has been shown that the net force exerted on a focal adhesion developing at spatial coordinate $\mathbf{x}$ varies depending on the growth/maturation stage of the developing focal adhesion [22]. As integrins bind and congregate in different cellular regions, they begin to accumulate more force. But a spatial coordinate may contain multiple developing stress fibers that each attach at different points within the cell. Hence, there may be multiple force components contributing to the net force being exerted at the given point. To account for this, the force equation incorporated several stages of focal adhesion development.

The earliest stage corresponds to the initiation of the cytoskeleton where force accumulation is dominated by integrin clustering, strengthening the adhesion and reinforcing the developing focal adhesion complex [23,24]. These components are only expected to significantly contribute to the net force at the early stage of focal adhesion development where building a sufficiently strong adhesion is necessary in order to construct stable myofibrils. Consequently, the adhesion strengthening mechanism was modeled as a bounded increasing function of the bound integrin density with a tunable parameter ρ_0 and direction $\hat{e}$

$$\mathbf{F}_{adh}(\mathbf{x}) = k_{CS}dA_{FA,p}\frac{\rho_b}{\rho_b + \rho_0}\hat{e} \tag{3}$$

Here, k_{CS} denotes the equilibrium adhesion force and $dA_{FA,p}$ is the minimum focal adhesion area required for a stress fiber to begin to form, typically of the order of nanometers [24,25] . The direction of the adhesive force vector, $\hat{e}$, was determined by leveraging that early on in myofibrillogenesis the cell is densely packed and interconnected [26]. As such, the force associated with the early-stage focal adhesion complexes may be approximated by assuming that all bound integrins contribute to initial force accumulation [14,16]. This approximation was incorporated by defining the average direction of the adhesive force using the vector sum of all contributions from all other integrins in the cell, $R(\mathbf{x})R(\mathbf{x}')\ [\mathbf{x}' - \mathbf{x}]$.

Once an adhesive area has been created, molecular interactions drive the recruitment of integrins to the growing focal complex [20]. To simplify, we assumed any integrin within the cell island may connect to any other integrin so long as both connectors have a sufficient adhesion force. This allowed the focal adhesion complexes to interact with each other and develop an initial dense cytoskeletal web [26] to aid in integrin recruitment and clustering. In this way, more bound integrins within a region are likened to an increase in focal adhesion area, a property that is known to be linked with increased force [19,20].

The description for the bound integrin recruitment force prior to the formation of myofibrils was developed based on the fraction of integrins contributing to force production at any appropriate point and the distance between the points under consideration [14]

$$\mathbf{F}_\rho(\mathbf{x},t) = \tilde{f}_\rho R(\mathbf{x})H(R(\mathbf{x}) - R_t)\int_\Psi R(\mathbf{x}')H(R(\mathbf{x}') - R_t)\hat{\mathbf{x}}d^2\mathbf{x}' \tag{4}$$

where $\hat{\mathbf{x}} = \mathbf{x}' - \mathbf{x}$, $H(\cdot)$ is the Heaviside function, R_t represents the fraction of bound integrins that must contribute to force in order to support a cytoskeletal connection, and $R(\mathbf{x})$ is the fraction of bound integrins that contribute to force production modeled using a Langmuir Isotherm

$$R(\mathbf{x}) = \frac{\rho_b(\mathbf{x},t)}{\rho_b(\mathbf{x},t) + \rho_0} \tag{5}$$

The inclusion of H and R restricted this force component to only affect spatial coordinates with a sufficiently large density of bound integrins. In practice, this term aids to bias early force accumulation toward regions of the cell with a high density of bound integrins. As more integrins accumulated within the various cellular regions, focal adhesions quickly began to assemble or disassemble as needed. A point within the simulated cell was classified as part of a focal adhesion if the force magnitude at that point was larger than a minimum threshold value. Based on the experimental literature, the amount of force generated is dependent on the size of the focal adhesion and maturation stage, increasing at a constant rate of 5.5 ± 2 nN/μm^2 [19,20,27]. With smaller focal adhesions having an area of the order of 1–2 μm^2 and larger focal adhesions having an area at least 5–8 μm^2, we estimated the amount of force needed in order for a premyofibril to begin forming to be approximately 3 nN. Any point with force magnitude meeting this threshold was termed an anchoring point.

Once the cytoskeletal force at two anchoring points met the minimum magnitude described above, the construction of a myofibril curve could begin. The adhesive region containing points capable of sustaining the construction of a myofibril was designated Ψ_{FA}, the set of all anchoring points. Depending on the likely stage of maturation of the myofibrils anchored at $\mathbf{x}$, the force contribution could be separated for the premyofibril stage ($\mathbf{F}_p$) and the nascent stage ($\mathbf{F}_n$)

$$\mathbf{F}_p(\mathbf{x},t) = \tilde{f}_p\int_{\Psi_{FA}} \Pi_p(\mathbf{x},\mathbf{x}')\frac{N_F(\mathbf{x},\mathbf{x}')}{N_{\text{tot}}}L_{\text{tot}}(\mathbf{x},\mathbf{x}')\hat{v}(\mathbf{x},\mathbf{x}')d^2\mathbf{x}' \tag{6}$$

$$\mathbf{F}_n(\mathbf{x},t) = \tilde{f}_n \int_{\Psi_{FA}} \Pi_n(\mathbf{x},\mathbf{x}') \frac{N_F(\mathbf{x},\mathbf{x}')}{N_{\text{tot}}} L_{\text{tot}}(\mathbf{x},\mathbf{x}') \hat{v}(\mathbf{x},\mathbf{x}') d^2\mathbf{x}' \quad (7)$$

As constructed, the two myofibril force contributions are dependent on the structure of the cytoskeletal network being constructed. In particular, $N_F(\mathbf{x},\mathbf{x}')$ denotes the number of myofibrils connecting $\mathbf{x}'$ and $\mathbf{x}$ so that N_F/N_{tot} identifies the fractional contribution of the connectors. This term allowed network density to play a role in force accumulation. The total length of the connections spanning $\mathbf{x}'$ and $\mathbf{x}$ was denoted by L_{tot}, which worked in concert with $\tilde{f}_p$ and $\tilde{f}_n$ to explore the relationship between net force and myofibril length (Sec. 2.6), and the direction of the force is specified by $\hat{v}$. Since it is difficult to identify the myofibril maturation stage without exploring the sarcomeric structure that makes up the myofibril, both stages were considered in this formulation with Π_p and Π_n denoting the probability that a myofibril connecting $\mathbf{x}$ and $\mathbf{x}'$ is classified as a premyofibril or nascent myofibril, respectively (Sec. 2.5). The net force associated with the focal adhesion at $\mathbf{x}$ was then described by the sum of the individual force components

$$\mathbf{F}(\mathbf{x},t) = \mathbf{F}_{adh}(\mathbf{x},t) + \mathbf{F}_\rho(\mathbf{x},t) + \mathbf{F}_p(\mathbf{x},t) + \mathbf{F}_n(\mathbf{x},t) \quad (8)$$

In practice, the force equation is dominated early on by the first two terms in Eq. (8) since the focal adhesion complexes need time to grow. This corresponds to $N_F(\mathbf{x},\mathbf{x}') = 0$ in $\mathbf{F}_p$ and $\mathbf{F}_n$. As the integrin density increases in different regions of the cell and the developing focal adhesions become reinforced, the force magnitude may begin to increase until reaching the minimum 3 nN threshold required in order to support the formation of a myofibril bundle. The collection of anchoring points Ψ_{FA} then becomes nonempty and myofibril bundles can be constructed by considering any two distinct anchoring points $\mathbf{x}$ and $\mathbf{x}'$. The following sections outline how the myofibril network is constructed once Ψ_{FA} becomes nonempty. Section 2.3 provides an overview of how an individual myofibril curve can be constructed in an energetically favorable way given any two anchoring points. This construction utilizes the location of the various anchoring points as well as the associated force vectors obtained through Eq. (8). However, not all possible individual curves are necessarily admitted into the overall network. An overview of how the network is populated using the individually constructed curves outlined in Sec. 2.3 is provided in Sec. 2.4.

2.3 Optimization Driven Construction for Individual Myofibrils. As outlined in Sec. 2.2, individual myofibril curves were constructed using designated anchoring points once a sufficient force magnitude was reached. Each myofibril was constructed as a fourth-order parametric Bézier curve whose bending energy could be described using a reparameterization of the standard bending energy equation [28]

$$E_B = \frac{l_p k_B T}{2L_c^3} \int_0^1 |r''(s)| ds \quad (9)$$

where $r(s)$ refers to the standard Bézier curve representation, L_c is the length of the curve, l_p denotes the persistence length of the curve, k_B is the Boltzmann constant and T is the absolute temperature in Kelvin [28,29]. The standard curve r was then described by designating control points $\mathbf{P}_0, \ldots, \mathbf{P}_4$ where $\mathbf{P}_0$ and $\mathbf{P}_4$ denote the starting and ending points for the curve. If the tangent vectors at $\mathbf{P}_0$ and $\mathbf{P}_4$ were written as $\hat{v}_1$ and $\hat{v}_2$, , respectively, the control points $\mathbf{P}_1$ and $\mathbf{P}_3$ would satisfy

$$\mathbf{P}_1 = \mathbf{P}_0 + \frac{|\mathbf{P}_4 - \mathbf{P}_0|}{\alpha_{\mathbf{P}_1} |\hat{v}_1|} \hat{v}_1 \quad (10)$$

$$\mathbf{P}_3 = \mathbf{P}_4 + \frac{|\mathbf{P}_4 - \mathbf{P}_0|}{\alpha_{\mathbf{P}_3} |\hat{v}_2|} \hat{v}_2 \quad (11)$$

where $\alpha_{\mathbf{P}_1}$ and $\alpha_{\mathbf{P}_3}$ are stochastic constants which help define the control polygon through which each curve can be constructed. For our purposes, requiring $\alpha_{\mathbf{P}_1}, \alpha_{\mathbf{P}_3} \geq 4$ yielded curves with bending motifs that were similar to those seen in experimental images.

By utilizing the Bézier curve equation, the bending energy was rewritten in terms of the curve control points [30] as

$$E_B = \frac{72 l_p k_B T}{L_c^3} \left(\frac{5}{6} |\mathbf{Q}_0|^2 + \frac{2}{3} |\mathbf{Q}_1|^2 + \frac{1}{6} |\mathbf{Q}_2|^2 \right) \quad (12)$$

where

$$\mathbf{Q}_0 = \frac{1}{\sqrt{30}} \left(-\sqrt{3}\mathbf{P}_0 + 2\sqrt{3}\mathbf{P}_1 - 2\sqrt{3}\mathbf{P}_3 + \sqrt{3}\mathbf{P}_4 \right) \quad (13)$$

$$\mathbf{Q}_1 = \frac{1}{\sqrt{30}} \left(2\mathbf{P}_0 - 3\mathbf{P}_1 + 2\mathbf{P}_2 - 3\mathbf{P}_3 + 2\mathbf{P}_4 \right) \quad (14)$$

$$\mathbf{Q}_2 = \frac{1}{\sqrt{30}} \left(\sqrt{5}\mathbf{P}_0 - 2\sqrt{5}\mathbf{P}_2 + \sqrt{5}\mathbf{P}_4 \right) \quad (15)$$

The proposed myofibril was constructed by determining the control point $\mathbf{P}_2$ that optimized Eq. (12), depending on whether the constructed curve interacted with the nucleus.

There are several ways in which to optimize Eq. (12) depending on the constraints that are to be enforced on the unknown control point $\mathbf{P}_2$. In the simplest case where we optimize in a length-independent manner with $\mathbf{P}_2 = (\mathbf{P}_{2,x}, \mathbf{P}_{2,y})$ having no additional constraints, the critical points of the bending energy equation can be computed by solving $\nabla_{\mathbf{P}_2} E_B = 0$ for $\mathbf{P}_2$ over the entire real plane. Doing so yields a closed-form solution that is at least locally optimal.

However, in general, the state of the network may influence whether an individual curve should try to avoid the nucleus. In this case, we may impose constraints on $\mathbf{P}_2$ by requiring that the curve passes through a specified point $\mathbf{P}_c$ on the outer edge of the nucleus. Doing so allows for $\mathbf{P}_2$ to be written in terms of $\mathbf{P}_c$ and some s^* between 0 and 1 where $r(s^*) = \mathbf{P}_c$. The optimization problem can then be rephrased in terms of finding the s^* that yields the best bending energy value [30,31]. It can be shown by rewriting $E_B(\mathbf{P}_2)$ as $E_B(s^*)$ that such a solution is guaranteed to exist, thus allowing for a definition of $\mathbf{P}_2$ that is locally optimal with respect to the optimization problem posed.

In particular, whenever a myofibril was proposed, it was first determined whether the associated Bézier curve crossed the 2-D circular region occupied by the nucleus. If it did not, then the curve was immediately considered for placement within the myofibril network, as in the first optimization problem described above. However, if the curve intersected with the nuclear region, an additional energetic cost was added due to supplemental height levels that were assigned to all points within the nuclear region (Eq. (17)) as designated by the level of nuclear influence (moderate or major). Rather than force the consideration of this myofibril curve, the network was allowed to decide which type of individual curve optimization problem was best suited for minimizing the total energy of the network. To determine whether the accumulated energetic cost resulting from the initial curve optimization problem was acceptable, two additional curves were proposed (one on either side of the nucleus) using the same curve input information but with the added condition that the Bézier curve must attempt to avoid the nucleus, as in the second optimization problem described above. This amounted to two different optimization problems being posed and resulted in a total of three viable curve options for placement. The optimization problem that yielded a curve whose inclusion was the most beneficial to the network at large was accepted for network placement.

2.4 Extending Optimization to a Myofibril Network. The myofibril network was built at each time-step by populating an

initially empty geometry with individual curves. This was accomplished in the following manner:

(1) Identify Ψ_{FA};
(2) Determine a collection of viable endpoint pairings from Ψ_{FA};
(3) Rank the endpoint pairings, defining the order in which the network would be built;
(4) Build individual myofibril curves for each endpoint pairing;
(5) Attempt to place each curve into the network according to the prescribed ordering from point 3.

The first point above consists of identifying the set of anchoring points as described in Sec. 2.2. The second and third points allow for the construction of a template network (or network motif) which identifies the collection of myofibril endpoint pairings and the order in which the network will be built. The template network can be interpreted as the theoretically idealized form of the myofibril network where specific endpoints have been identified and are connected using straight myofibrils, the most energetically efficient individual curve from our construction since it has zero bending energy. Point four constructs the individual myofibril curves given endpoints $\mathbf{x}$ and $\mathbf{x}'$ as outlined in Sec. 2.3 and the final point uses the individual curves to build the full network following the ordering dictated by the template network.

To build the template network, the collection of all possible myofibril endpoints $\{(\mathbf{x}, \mathbf{x}')\}$ was created using the pairwise combination of all anchoring points from Ψ_{FA}. This set was then filtered to create a collection of viable endpoint pairings such that $\mathbf{F}(\mathbf{x})$ and $\mathbf{F}(\mathbf{x}')$ did not point in the same direction and the endpoints were not too close together, since such cases would result in myofibril curves that are biologically impossible. This template network construction and filtering process is visualized schematically in Fig. 1 by the first box under "Network assembly." To determine the order in which the network would be constructed, the remaining pairings were then ranked according to the angular similarity of their force vectors: $|\theta(\mathbf{x}, \mathbf{x}') - \theta(\mathbf{x}', \mathbf{x})|$ where $\theta(\mathbf{x}, \mathbf{x}')$ is the angle between the vectors $\mathbf{F}(\mathbf{x})$ and $\mathbf{x}' - \mathbf{x}$. The remainder of this section will focus on point five concerning the incorporation of individual myofibril curves into a fully realized network.

To build the myofibril network, the energetic cost of constructing an individual myofibril (Eq. (12)) and the energetic cost of placing the constructed myofibril in the cell were utilized to determine the total energy within the network

$$E^*_{\text{sys}} = \sum_{f_k} [(E^*_B(f_k) - E^{\max}_B(f_k)) + E^*_{\text{def}}(f_k)] \tag{16}$$

where f_k denotes the kth myofibril constructed. A constructed curve was accepted into the network if its inclusion contributed to reducing the total energy of the system. The energetic cost of constructing a myofibril was described by the first summation quantity in Eq. (16), which utilized the normalized form of the simplified bending energy equation (Eq. (12)), $E^*_B = E_B/(k_B T)$.

The second summation term, $E^*_{\text{def}}(f_k)$, accounts for the energetic change in placing a myofibril within an existing network. By likening the network of myofibril curves to a deformed planar surface with ridges defined by the spatial coordinates of the various curves, the inclusion of a newly constructed myofibril would constitute a deformation to the current surface. This was modeled using the equation for planar deformations as applied to a membrane with prescribed bending modulus κ_b and tension τ [32]

$$E^*_{\text{mem}}(\mathbf{x}|f_k) = \frac{\kappa_b}{2}\left(\nabla^2 h(\mathbf{x}|f_k)\right)^2 + \frac{\tau}{2}(\nabla h(\mathbf{x}|f_k))^2 \tag{17}$$

In our formulation, the membrane height h at a given spatial coordinate $\mathbf{x}$, as determined by the presence of the kth myofibril f_k, was approximated as the cumulative height of stacked myofibrils within the lattice discretization area dA around $\mathbf{x}$. That is to say, if myofibril f_k was constructed and passed near the lattice point $\mathbf{x}$, then $h(\mathbf{x}|f_k)$ was approximated as the product of the total number of myofibrils that pass near $\mathbf{x}$ in the current myofibril network (including f_k) and the diameter of an individual myofibril. To make our energy model more robust to changes in discretization area (Sec. 2.7), the total energetic change is scaled relative to the cell area of interest. The total energetic change that amounts from

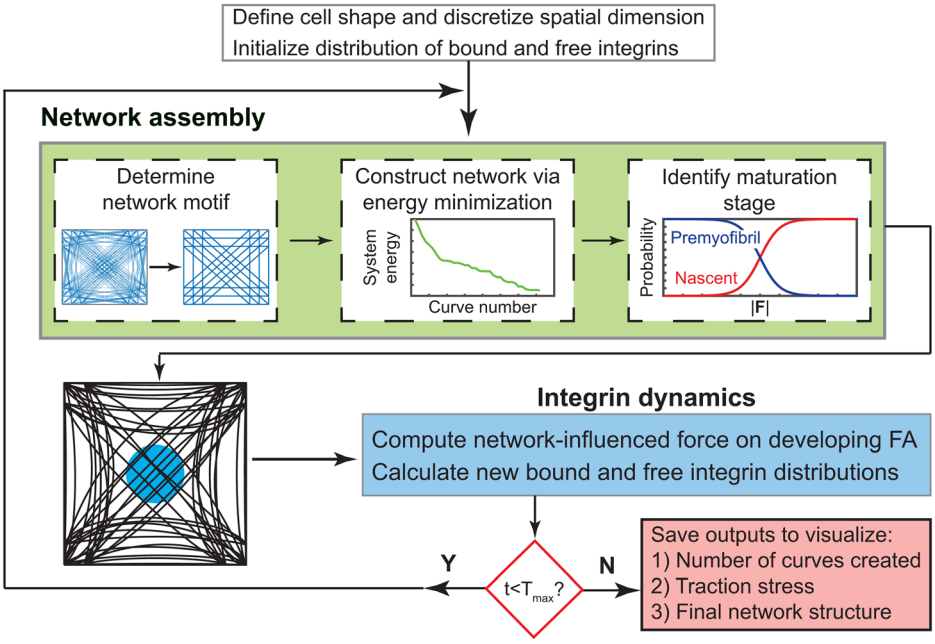

Fig. 1 Schematic overview of major modeling components. Basic model implementation consists of an initialize stage where the cell geometry is predetermined and required parameters are set. The initial distributions of bound and free integrins are determined and the different model components are carried out as outlined in Sec. 3.1.

incorporating a new myofibril into an existing network, normalized to the initial cell area, is defined as

$$E^*_{\text{def}}(f_k) = \frac{1}{A}\int_{\Psi}\left[E^*_{\text{mem}}(\mathbf{x}'|f_k\text{placed}) - E^*_{mem}(\mathbf{x}'|f_k\text{notplaced})\right]d^2\mathbf{x}' \tag{18}$$

2.5 Myofibril Maturation Designation. Once the cytoskeletal network was determined, each constructed curve was classified as either a premyofibril or nascent myofibril. The maturation process was assumed to be force-induced since there are suggested correlations between myofibril type, focal adhesion size, and the force generated by a myofibril [19,27]. As outlined in Sec. 2.2, we required both anchoring points to generate a sufficient force, denoted here by $\mathbf{F}^*$. While all myofibrils were initially designated premyofibrils, they could be reclassified as nascent myofibrils once enough force was generated. To ensure a transition between these two stages, a secondary force threshold $\mathbf{F}_c$ was incorporated whereby the probability of being classified as a premyofibril would begin to decrease once the secondary force threshold was passed.

To this end, we set $\mathbf{F}_{\min} = \min(|\mathbf{F}(\mathbf{x})|, |\mathbf{F}(\mathbf{x}')|)$ and modeled maturation as a second-order phase transition [33] where the energetic cost of maintaining the constructed curve in the premyofibril or nascent myofibril stage was described as

$$E^*_p = \begin{cases} E^*_B & \text{if } \mathbf{F}_{\min} \geq \mathbf{F}^* \\ 0 & \text{if } \mathbf{F}_{\min} < \mathbf{F}^* \end{cases} \tag{19}$$

$$E^*_n = \begin{cases} E^*_0 - \dfrac{(a^*)^2}{4b^*}\left(\dfrac{1}{\mathbf{F}_{\min} - \mathbf{F}^*} - \dfrac{1}{\mathbf{F}_c}\right)^2 & \text{if } \mathbf{F}_{\min} \geq \mathbf{F}_c \\ E^*_0 & \text{if } \mathbf{F}^* \leq \mathbf{F}_{\min} < \mathbf{F}_c \\ 0 & \text{if } \mathbf{F}_{\min} < \mathbf{F}^* \end{cases} \tag{20}$$

where E^*_0, a^*, and b^* are tunable parameters designed to make it more energetically beneficial to start as a premyofibril and mature to a nascent myofibril once the myofibril can maintain a desired amount of force. For consistency, E^*_p and E^*_n were written in terms of the force magnitude being continuous on $[0, \infty)$. However, during model implementation, these terms only contributed once a myofibril was able to form and be designated as a premyofibril or a nascent myofibril. The maturation energies were then used to determine the probability that a curve was in a given state of maturation:

$$\Pi_p = \frac{1}{1 + e^{-\Delta E^*}} \tag{21}$$

$$\Pi_n = \frac{1}{1 + e^{\Delta E^*}} \tag{22}$$

where $\Delta E^* = E^*_n - E^*_p$. In practice, the probability equations dictated that newly created myofibrils were designated as premyofibrils exclusively ($\Pi_p \approx 1$ and $\Pi_n \approx 0$), resulting in only a premyofibril force contribution in Eq. (8). As the simulation progressed and net forces began to accumulate, the secondary force threshold was passed and there was a transition that occurred where Π_p began to decrease and Π_n began to increase, resulting in a total increase in net force. This continued until late in the simulation, by which time all developed myofibrils were classified as nascent myofibrils ($\Pi_p \approx 0$ and $\Pi_n \approx 1$) and it became energetically unfavorable to incorporate new myofibrils into a well-developed network.

2.6 Incorporating Fiber-Length Dependence. Since there were three force constants within the force equation (Eq. (8)), we expect them to all have the same units as each integral term was meant to have a similar meaning. This implied that $\tilde{f}$ has units Pa/m, which we interpreted as the stress exerted on developing/maturing focal adhesion relative to an effective length. Previous studies have shown that there is constant stress exerted on focal adhesions of $T_{\text{est}} = 5.5 \pm 2$ nN/μm^2 [19]. This prescribes traction stress values (and hence, force magnitudes) at the ends of the myofibril bundles. These forces propagate from one end of the myofibril bundle to the other but how exactly that happens, i.e., how much stress each sarcomeric segment endures and how it's handled from segment to segment, has not been entirely explored. However, previous models have demonstrated that the organization of the myofibril network may be more qualitatively similar to experimental results when the force term is fiber-length dependent [14]. We incorporated this length-dependent behavior into our $\tilde{f}$ parameter

$$\tilde{f} = \frac{\{\text{Stress exerted on a } FA\}}{\{\text{Effective myofibril length}\}} \tag{23}$$

where the effective myofibril length was determined by the geometry of the cell. Specifically, the equation was formed by considering the number of sarcomeric segments that make up the longest possible myofibril and the average sarcomeric segment length. With this, we considered two specific dependency types: absolute-length dependence and relative-length dependence. In absolute-length dependence, the stress exerted on a focal adhesion was transmitted without loss along every sarcomeric segment independent of cell shape. On the other hand, in relative-length dependence, the stress was not transmitted between segments with perfect efficiency and would degrade based on the number of segments comprising the length of the longest myofibril. Specifically, this length term, if applicable, was set to be the maximum length of a straight myofibril within the prescribed cell geometry, $L_{\max}$. With this inclusion, the force term varied based on the type of length dependence

$$\tilde{f} \propto \frac{T_{\text{ext}}}{N^{\alpha}_{\text{seg}} L_{\text{seg}}} = \frac{T_{\text{est}}}{L^{\alpha}_{\max} L^{1-\alpha}_{\text{seg}}} \tag{24}$$

In this formulation, α is the dependency parameter with value 0 or 1, N_{seg} refers to the maximum number of sarcomeric segments that make up the myofibril having length $L_{\max}$ and L_{seg} denotes the average segment length (approximately 2 μm [34,35]). The three-length-related quantities satisfy the equation $N_{\text{seg}} \approx L_{\max}/L_{\text{seg}}$. Setting $\alpha = 0$ would create an absolute-length dependence where $\tilde{f}$ is constant regardless of cell geometry, and $\alpha = 1$ would create a relative-length dependence where $\tilde{f}$ varies depending on cell shape changes.

2.7 Model Discretization. Following designation of the cell geometry, initial integrin density distribution, and nuclear properties, the model was discretized in space and time. For the given cell geometry, spatial points along and within the cell boundary were determined by uniformly discretizing the cell region using a minimum of 120 spatial points. Each point was then assigned a lattice discretization area, dA, defined as the ratio of the specified cell area and the total number of discretization points created. The distribution and number of spatial points were chosen to sufficiently cover the cell area geometry. A total of 72 h of simulated time was considered for each run of the model with time steps of the order of minutes, consistent with the timeframe needed for cytoskeletal structures to form [26].

2.8 Fibronectin Patterning. Large, rectangular cover glass (Brain Research Laboratories, Newton, MA) was sonicated, then spin-coated with 10:1 Polydimethylsiloxane (PDMS; Ellsworth Adhesives, Germantown, WI). The coated glass was placed in a

60 °C oven to cure overnight and then cut into, approximately, 13 mm x 15 mm rectangular coverslips to fit in a 12-well plate. Fibronectin (FN; Fischer Scientific Company, Hanover Park, IL) was patterned onto the coverslips to have islands of a variety of shapes with areas of 1250 μm^2 or 2500 μm^2 using microcontact printing, as previously described [8,36]. The FN-patterned coverslips were placed in a solution of 5 g Pluronics F-127 dissolved in 0.5 L sterile water for 5 min and rinsed three times with room temperature phosphate-buffered saline 97 (PBS; Life Technologies, Carlsbad, CA) in order to block the cells from attaching outside of FN lines.

2.9 Neonatal Rat Ventricular Myocyte Cell Culture. As previously described [8,36,37], neonatal rat ventricular myocardium was extracted from two-day-old Sprague Dawley rats (Charles River Laboratories, Wilmington, MA) in agreement with the guidelines of the Institutional Animal Care and Use Committee of University of California, Irvine (Protocol No. 2013-3093). The cardiomyocytes were then isolated from the ventricular myocardium as previously described [8,36,37]. Cells were counted and seeded onto FN coated coverslips at a density of 1 M cells per well in a 6-well plate and 400 K per well in a 12-well plate. After 24 h, dead cells were washed away with PBS and the remaining cells are fed with 10% FBS M199 culture media. Another 24 h later, the 10% M199 was replaced with warm 2% FBS M199 culture media.

2.10 Fixing, Immunostaining, and Imaging. Cells were fixed with warm 4% paraformaldehyde (Fisher Scientific, Hanover Park, IL) supplemented with 0.001% Triton X-100 (Sigma-Aldrich, Inc., St. Louis, MO) in PBS for 10 min, as previously described [8,36,37]. Cultures were then immunostained for actin (Alex Fluor 488 Phalloidin; Life Technologies, Carlsbad, CA), sarcomeric α-actinin (Monoclonal Anti-α-actinin; Sigma Aldrich, Inc., St. Louis, MO), nuclei (4′,6′-diaminodino-2-phenlyinodol (DAPI; Life Technologies, Carlsbad, CA), and FN (polyclonal rabbit antihuman fibronectin; Sigma Aldrich, Inc., St. Louis, MO), as previously described [8,36,37]. Secondary staining was applied using tetramethylrhodamine-conjugated goat antimouse IgG antibodies (Alexa Fluor 633 Goat antimouse or Alexa Fluor 750 Goat antimouse; Life Technologies, Carlsbad, CA) and goat antirabbit IgG antibodies (Alexa Fluor 750 goat antirabbit or Alexa Fluor 633 Goat antirabbit; Life Technologies, Carlsbad, CA). The images were collected using an IX-83 inverted motorized microscope (Olympus America, Center Valley, PA) with an UPLFLN 40× oil immersion objective (Olympus America, Center Valley, PA) and a digital CCD camera ORCA-R2 C10600-10B (Hamamatsu Photonics, Shizuoka Prefecture, Japan).

2.11 Image Analysis. Image analysis of experimental data and model simulations was performed using previously created custom MATLAB codes [8,36]. Structural comparisons were made by computing the co-orientational order parameter (COOP) for each cell pair. Because the COOP allows for comparisons at multiple spatial scales, the model-generated networks, and experimental cells were compared using several different spatial scales. This was done so that both global and local structural behavior could be compared. Images were segmented into grids and the length of each grid square could vary from 1 μm to approximately 50 μm. The COOP ranges from 0 to 1 and is determined by computing the maximum eigenvalue of the structural tensor, as previously described [36].

All experimental data utilized for computational analysis and model comparisons were previously published [8,38]. In each case, the single cells were analyzed for key cellular properties including, but not limited to, having single nuclei (to ensure a single cell was considered), being fully attached and spread on the ECM island, demonstrating good actin and α-actinin staining, and showing fully realized cytoskeletal structures like sarcomeres. We refer the reader to these individual publications for sample experimental images.

2.12 Statistical Analysis. Results are expressed using the mean with error bars representing the standard deviation. One-way analysis of variance (ANOVA) with the Tukey-Kramer test for pairwise comparisons was used to determine statistical significance. A p-value less than 0.05 was considered statistically significant.

3 Results

3.1 Model Overview. While the cytoskeleton consists of several different components, we focused on specific contraction-related portions of the cytoskeletal network. In particular, to explore the development and maturation of the myofibrillar component of the sarcomere-based cytoskeletal network, our model consisted of two interacting components, which allowed for the visualization of myofibril curves within a simulated 2-D cell geometry (Fig. 1. A focal adhesion refers to a collection of proteins that interact to form a linkage between the actin stress fibers and extracellular matrix [21,39]. Focal adhesions assemble due to the interactions between cell surface integrins and an assortment of proteins and they grow via integrin accumulation through actin polymerization and increased tension force [21]. These adhesive structures can disassemble during cell migration and spreading [21,39] due to alterations in talin density or actin reorganization. Of the numerous focal adhesion-associated proteins, integrins are particularly dominant and are present in several different cellular processes due to the many different types of integrin subunits [40]. As such, we modeled the focal adhesion dynamics by considering the density of integrin proteins. Specifically, we focused our attention on dynamics relating focal adhesion proteins to mechanotransduction. This approach allowed the model to capture the critical properties associated with focal adhesion dynamics: assembly, disassembly, and maturation.

Focal adhesions were modeled using kinetic equations by considering the density of bound and unbound integrins, ρ_b and ρ^*, respectively (Eqs. (1)–(2)). At each point in the cell containing some density of bound integrins, a net force **F** (Eq. (8)) was exerted, which accounted for adhesion reinforcement via integrin clustering and the influence of the forming or maturing cytoskeleton. Once a minimum density of bound integrins was present and contributing a force magnitude sufficient enough to sustain a cytoskeletal connection, a premyofibril could be created.

To assemble the cytoskeletal network, the collection of viable anchoring points were identified and a template network was determined based on the net force vectors associated with each point. This template network defined the order in which the individual curves would be created. The probability of a constructed curve being at a particular stage of maturation was assumed dependent on the amount of force generated at the endpoints of the curve, with premyofibrils having smaller forces while larger forces indicated maturation into the nascent myofibril stage (Eqs. (21)–(22)). The densities of free and bound integrins at each time-step would respond to the cytoskeletal network that was constructed through a force-induced integrin recruitment term. In this way, developing focal adhesions would be reinforced allowing for more myofibrils to be constructed. This would influence the net force exerted on the focal adhesions resulting in more integrins being recruited to the focal adhesion sites where the cycle would repeat.

While individual myofibrils may be anchored to the extracellular matrix through focal adhesions, this consideration alone is not sufficient to build a complete cytoskeleton since the eventual network structure that is formed interacts with various internal cellular components. Most prominent of which is the nucleus. Indeed, it has been shown that the nucleus plays a role in cell migration

due to its physical interaction with the dynamic cytoskeleton [41]. There is even evidence that the nucleus can elastically deform when cell geometry is altered due to the compressive force being exerted on the nucleus by the cytoskeleton [42]. This remodeling in nuclear shape is accompanied by alteration in other nuclear properties such as changes in nuclear volume and elastic modulus. While the presence of the nucleus has been linked to cytoskeletal dynamics, its overall influence in the initial construction of the cytoskeleton has been less clear. To explore this, the model incorporated the physical location and amount of nuclear interference in cytoskeletal construction by considering the nucleus as a fixed obstacle for the network to interact with.

Individual myofibrils were modeled as fourth-order Bézier curves [43] with minimal bending energy. This was accomplished by identifying the starting and ending points for each curve according to the criteria described above. A net force vector **F** was associated with each point and used to determine the tangent vector to the curve at the designated point. The remaining control

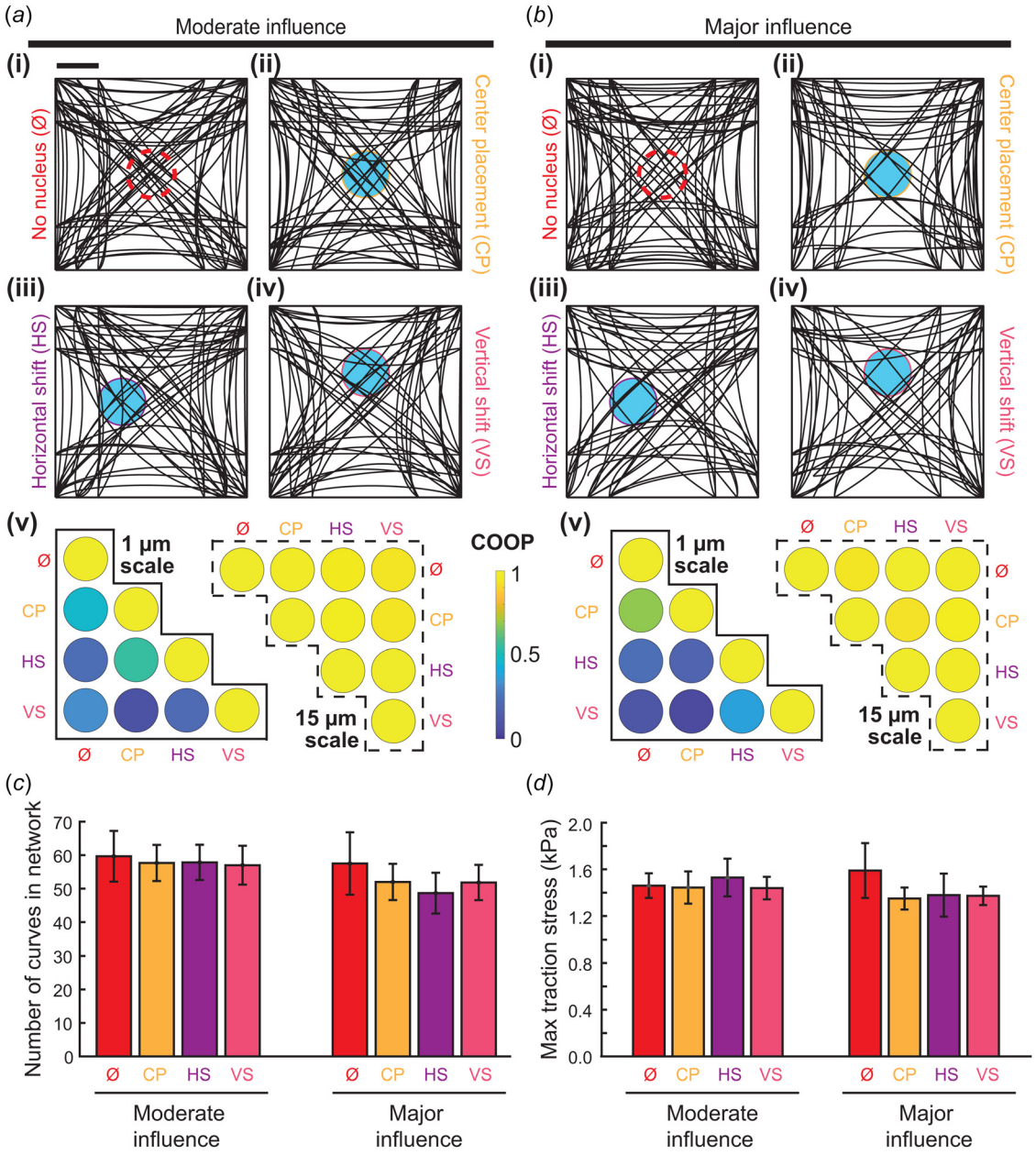

Fig. 2 Influence of the nucleus on cytoskeletal properties. The nucleus was provided a level of influence on the cytoskeleton corresponding to the energetic cost of creating a curve that passes over the nucleus. This level of influence varied from moderate (*a*) to major (*b*) with levels likened to a more elastic or more stiff nucleus, , respectively. The location of the nucleus was altered to mimic the cases where there was no nucleus present (i, Φ), placed in the geometric center position (ii, CP), placed using a horizontal shift of 7 μm left of center (iii, HS) or placed using a vertical shift 7 μm above the center point (iv, VS). The exact placement of the nucleus was fixed at the start of each simulation. The COOP was applied at two different length scales to the networks obtained (v). After performing 6 simulations of each nucleus location in (*a*) and (*b*), the average number of curves created over all simulations was recorded (*c*) as well as the maximum traction stress (*d*), estimated using the magnitude of the net force at every point in the cell divided by unit cell area. Scale bar: 10 μm.

points defining the parametric curve were determined based on the endpoint tangent vectors and how to most effectively minimize the bending energy equation (Eq. (12)). To determine whether the constructed curve was viable, an energetic cost associated with placing a proposed curve within a developing network was included (Eq. (18)). By taking into account the energetic cost of constructing a myofibril coupled with the potential energetic cost of placing the constructed myofibril in the cell, only curves that contributed to the minimization of the system energy (Eq. (16)) were utilized to construct the cytoskeletal network.

3.2 Impact of the Nucleus on the Cytoskeleton. Since the model allowed for the nucleus to influence the development of the cytoskeleton, we explored how the final network might be impacted by changes in the location and relative influence of the nucleus. To match available experimental data, the simulated cell was given a square geometry with 2116 μm^2 cell area. While not naturally occurring, this shape can be made in vitro [8,38] and provides a good baseline for parameter fitting and demonstrated a critical component of cytoskeletal formation: the overall motif of having curves that predominately span the direction of elongation (horizontally, for our setup) can be broken if the right shape is chosen. The symmetries of a square (horizontal, vertical, and diagonal) provided a way to test that the model is able to adapt to different geometries through the force-mediated mechanisms rather than modeling the cell shape explicitly. At the start of each simulation, the nucleus was placed at a specified location and assigned a level of influence (moderate or major). Depending on the influence level, the energetic cost of constructing individual myofibrils that would have to interact with the nucleus was altered. These levels are analogous to different elastic moduli for the nucleus with, for example, moderate influence being likened to a lower elastic modulus leading to a more compressible nucleus that can interact with many curves before substantially adding to the system energy.

As a baseline for comparison of nuclear influence levels, the nucleus was removed entirely from one set of simulations (Figs. 2(*a*), 2(*b*)(i)). Figures 2(*a*), 2(*b*)(i)–(iv) depict representative examples for each case, which consisted of six simulations where the nucleus location and level of influence were prescribed. In each simulation, the initial distribution of integrins was randomized. The nucleus was then placed in three different locations within the cell geometry and the resulting cytoskeletal networks were evaluated. This was done in the cases where the nucleus was allowed a moderate level of influence on the cytoskeleton (Fig. 2(*a*)(ii)–(iv)) and when the nucleus was allowed a major level of influence on the cytoskeleton (Fig. 2(*b*)(ii)–(iv)). From the results of the simulations, it can be qualitatively observed that the presence of the nucleus impacts the behavior of the network near the nucleus location. When no nucleus was present, there was an increase in straight diagonal curves passing near the geometrical center of the cell. However, when the nucleus was taken into account, it became more energetically favorable to create curves that bended around the nucleus rather than go across it. As might be expected, the level of nuclear influence impacted the total energetic cost of creating the network. This could be seen qualitatively by the apparent decrease in the number of curves created for each nucleus location.

The change in cytoskeletal structure for each level of nuclear influence was quantified using the Co-Orientational Order Parameter (COOP) [36], where all cell pairs were considered (Figs. 2(*a*), 2(*b*)(v)). This metric ranges from zero to unity and quantifies the level of consistency between pairs of structures. A COOP of one indicates the structures perfectly mimic each other while a value of zero means there is no consistency between the two structures. The metric can be calculated for different length scales, allowing for structural comparisons at a local level when a small length scale is designated while more global comparisons could be captured by using a large scale. Calculating the COOP at a large ($\sim$15 μm) length scale revealed high levels of global consistency regardless of nucleus placement. At a small ($\sim$1 μm) length scale, structural differences became more apparent. This could suggest that the mechanisms underlying the interaction between the cytoskeleton and the nucleus may be central to producing local variations in cytoskeletal networks experimentally. However, this may not hold true for elongated cells where there is less space for the myofibril bundles to occupy, resulting in more locally consistent structures. This could indicate that the level of influence of the nucleus might vary from cell to cell due to other intracellular factors.

The impact associated with changing the amount of nuclear influence on the cytoskeleton was further quantified by performing multiple simulations where the nucleus location was changed. Due to the difference in resulting cytoskeletons for each scenario, the average number of curves created in each case was considered (Fig. 2(*c*)) as well as the average maximum traction stress generated (Fig. 2(*d*)). Consistent with qualitative observations, there was a general decrease in the average number of curves created when nucleus placement was fixed and level of influence was increased. Similarly for the average maximum traction stress, which was computed at the end of each simulation by evaluating $|\mathbf{T}(\mathbf{x})| = |\mathbf{F}(\mathbf{x})|/dA$, where dA represents the lattice discretization area (see Sec. 2.7), at every spatial coordinate $\mathbf{x}$ of the discretized cell and determining the maximum value, $|\mathbf{T}|_{\max} = \max_{\mathbf{x}}|\mathbf{T}(\mathbf{x})|$. Under all scenarios, the model consistently produced maximum traction stress values within the typical range reported experimentally [17]. However, these differences were not statistically significant. Since there were no statistically significant differences in these cases and the nucleus is expected to play a larger role in elongated cells, a moderate level of nuclear influence was assumed for the remaining simulations. This allowed cytoskeletal networks to be created in rectangular geometries with variable aspect ratios.

3.3 Exploring Force-Length Dependence. There has been evidence suggesting that the force exerted on developing focal adhesions may be tied to the cell geometry via a force-length relationship [15,19]. Previous modeling has shown that in cells with geometries defined by several different lengths, a force-length relationship is likely to produce cytoskeletal networks more consistent with experimental findings compared to no force-length dependence [14]. However, identifying potential types of dependence requires the inclusion of length scales. Since our model is dimensionalized, it was used to explore two potential force-length relationships that may be applicable. The force equation consists of terms that scale with fiber length, designated $\tilde{f}$ (Eq. (23)). While this value is fixed for each geometry, the parameter α can be tuned to either 0 or 1, each representing a different type of force-length dependence. When $\alpha = 0$ (OFF), the force parameters maintain a consistent value for all shapes. This causes the force to be dependent on an absolute-length value. When $\alpha = 1$ (ON), the force parameters are allowed to vary based on the maximum end-to-end fiber length within a cell geometry. Under this formulation, the force parameter values are scaled as a result of the changing cell geometry, which was classified as a relative-length dependence.

Multiple simulations were run on geometries with fixed cell area but different aspect ratios. To remain consistent with the experimental data, the simulated cells were given the same cell area as in the experiments (2116 μm^2), and the aspect ratios varied from 1:1 (square) to 13:1 (highly elongated rectangle), in line with the ratios used for the experimental cells. In each simulation, the nucleus was randomly placed near the center of the geometry and allowed to have a moderate level of influence. For each aspect ratio, the number of curves and corresponding curve lengths were recorded along with the final maximum traction stress predicted by the model. There was a decrease in the average number of curves present in the final network for both force-length

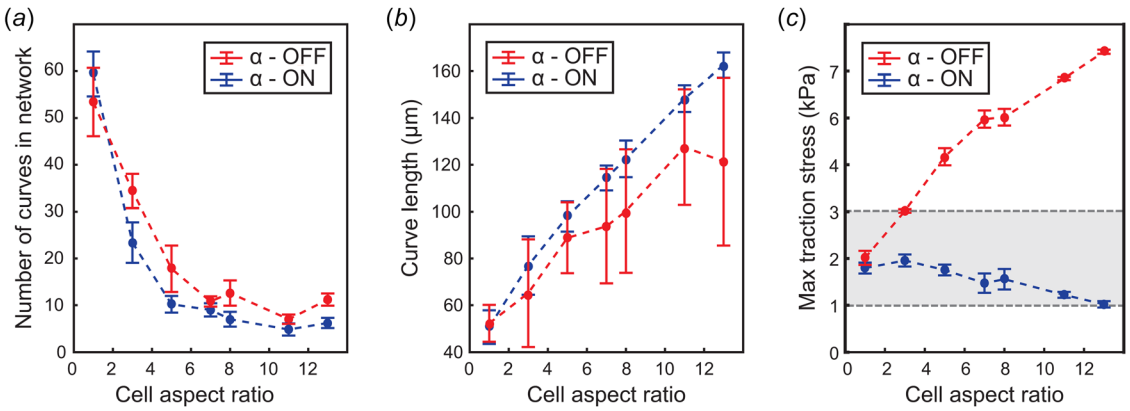

Fig. 3 Testing length-dependence relationships. Model was implemented on rectangular geometries with aspect ratios varying from 1:1 to 13:1. For each aspect ratio, six simulations were performed and α was set to $\alpha = 0$ OFF: absolute-length dependence) or $\alpha = 1$ (ON: relative-length dependence). The average number of curves created (*a*), the average curve length (*b*), and the average maximum traction stress (*c*) were computed for each aspect ratio. The shaded region identifies the range of average maximum traction stress values reported from the literature.

relationships explored (Fig. 3(*a*)). Increasing aspect ratio also resulted in longer curves being generated on average, with more consistent curve lengths observed in the relative length-dependence scenario (Fig. 3(*b*)). Overall, these results are consistent with what can be qualitatively observed in experimental cells [17,44,45]. However, there is a behavioral shift that occurs when considering the average maximum traction stress that is produced (Fig. 3(*c*)). Simulations utilizing the relative-length dependence produced traction stress values between ~1 and 2 kPa, within the 1 and 3 kPa range reported for cells having these aspect ratios [17]. In contrast, simulations with the absolute-length dependence produced traction stress values that increased almost linearly with aspect ratio. This scenario almost universally produced traction stress values that were outside the physiological range. When coupled with the wide variability in curve lengths produced, a mechanism causing the force exerted on a focal adhesion to vary in this type of length-dependent manner seems unlikely. Therefore, for all other comparisons presented, a relative-length dependence ($\alpha = 1$) is assumed.

3.4 Structural Consistency in Experimental and Simulated Networks. Previous studies have reported that increasing cell aspect ratio results in an increase in intracellular alignment [44,45]. The increase in alignment correlates with cytoskeletal networks having similar internal architecture and has been previously quantified using the COOP metric [8]. To test the viability of the model, this metric was applied to model-generated networks for different cell geometry aspect ratios. The model is able to capture important qualities present in some experimental cells. Comparing a sample model simulated cell with an experimental cell (Figs. 4(*a*), 4(*b*)), overall architecture is qualitatively similar. Of particular interest is the presence of myofibrils that do not align with the overall direction of the network. Due to the spatial discretization used in the model implementation, this feature is more noticeable in the model simulation (Fig. 4(*b*), left boundary in simulated cell). However, this is not a modeling artifact as similar behavior can be found in some experimental cells (Fig. 4(*a*), left boundary of experimental cell). Furthermore, there are clear endpoints visible in the model-generated networks because of the spatial discretization used which allows for myofibrils that do not terminate on the cell boundary. This phenomenon of myofibrils beginning or ending at points within the interior of the cell is also present in some experimental cells although it is much less pronounced due to the large density of myofibrils and potential imaging restrictions. Additionally, the influence of the nucleus can be seen in both the model-generated network and the experimental cell. Both images depict some myofibrils passing directly over the cell center while others avoid the region entirely. This is representative of the cell's desire to avoid overcrowding around the nucleus.

In experimental cells, the COOP was seen to monotonically increase as the cell was elongated (Fig. 4(*a*)), demonstrating that aspect ratio influences the structural consistency of the cytoskeleton at both the small and large scales. When applied to model-generated networks, a similar trend was observed (Fig. 4(*b*)). At both length scales, the simulations demonstrate an increase in structural consistency as the cell geometry elongates.

Experimental cells were then grouped alongside the model-generated networks for each aspect ratio. Computing the COOP using the grouped data revealed a similar trend as the experimental data alone (Fig. 4(*c*)). This was further analyzed to determine whether the simulated networks could be distinguished from the experimental data. Accordingly, the group consisting of only experimental cells was used as a baseline. Previous results have demonstrated that in individual cells, the COOP varies depending on the length scale chosen with an inflection point around the 3–4 μm scale [8]. To test whether length scale might influence the viability of the model results, a 3 μm scale was included in the analysis. The fitted Hill functions for all data sets were plotted along with the 95% confidence band of the baseline group (Fig. 4(*d*)). When viewed together, the fitted functions for most data sets fell within the confidence region across the length scales analyzed. Notably, the group model/experiment dataset fell within the confidence region for nearly all aspect ratios. These results demonstrate that the model-generated networks are structurally consistent with the experimental data for a variety of aspect ratios at different length scales.

4 Discussion

The cytoskeleton interacts and coordinates with numerous intracellular structures across several length scales [1,8,10]. As the cytoskeleton develops, the dense packing induces a physical competition for space between neighboring myofibril bundles. This also causes the cytoskeletal network to interact with other subcellular structures that occupy space within the cell such as the nucleus [41]. Until now, no technique had been developed that took into account spatial constraints to predict the exact placement of myofibril bundles within a cell. We addressed this by developing a theoretical model that used basic structural components to build a dynamically changing cytoskeletal network. We simulated the maturation pathway experimentally using immature NRVMs capable of attaching and spreading on ECM islands with

designated geometries. By using NRVMs that had yet to reach full maturation and have not lost their plasticity, we were able to compare individual cardiomyocytes containing identifiable internal structures [8,38] with model-generated structures constructed using an equation-driven representation of the maturation process.

The model presented successfully accounts for the orientation and bending of myofibrils and produces explicit traction forces measurement predictions. This allowed for both qualitative and, more importantly, quantitative comparisons between model predictions and experimental measurements. Since the model explicitly utilizes the relative scale and dimensionality of various parameters and variables when describing cytoskeletal interactions, we are able to produce numerical predictions in a way that nondimensional models have not been setup to address. Fundamental to the model is a focus on the force equation as a means for recreating experimentally observed behavior. In fact, past experiments have demonstrated a relation between a cell's elongated length and the change in force [19,46]. Being able to capture this relation with units intact in a way that allows for direct comparison between differently shaped cells is an important first step to exploring potential mechanisms that may be at play.

Our approach differs from previous attempts in several crucial aspects. Typically, cytoskeletal components are studied in isolation [47–49] and when multiple components are combined, the emphasis is often placed on how contractility might influence the normalized traction stress magnitudes in different cellular regions [13,50]. Our model links several structural components allowing for direct exploration of network properties including the impact of nucleus location on a developing cytoskeleton (Fig. 2). Additionally, since most models take a nondimensional approach [13,14], the nature of the myofibril force-length dependence had not been fully explored. The force equation (Eq. (4)) was developed with parameters that incorporated length scales, making it possible to investigate whether dimension-dependent force-length

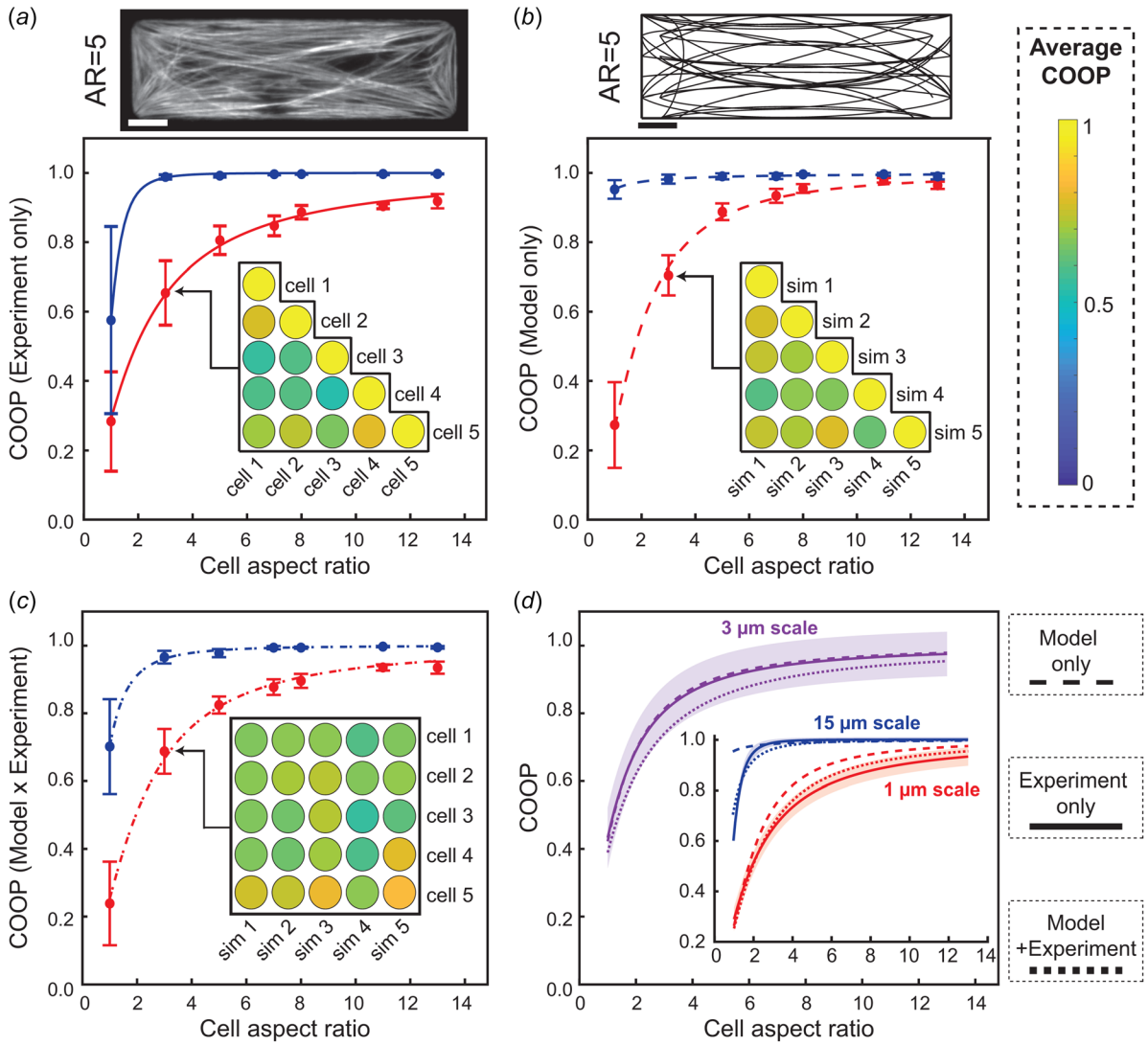

Fig. 4 Testing structural consistency. The average COOP was computed at small (~1 μm) and large (~15 μm) scales for experimental cells (*a*) and model-generated networks (*b*). At each aspect ratio, experimental cells and model simulated networks were combined into a single group and the average COOP was computed (*c*). The COOP was recorded within each aspect ratio by comparing all possible cell-cell pairs (*a*, *b*, *c* insets). For the 3 μm length scale, networks generated by the model simulations were combined with experimental cells into a single group and the corresponding COOP values (dotted lines) were computed (*d*). The group containing only experimental data (solid lines) and the group containing only model networks (dashed lines) were also computed for comparison. This was repeated at both the small and large length scales (*d*, inset). The shaded areas designate the 95% confidence region for the experiment only group. Scale bars: 10 μm. All analysis was performed using previously published experimental data (see Refs. [8,38]) .

relationships influenced cytoskeletal construction (Figs. 3(*a*), 3(*b*)). Previous studies have demonstrated that cell contractility varies within 1–3 kPa [15,17], which our model is able to capture using only the feedback between the distribution of focal adhesions and the developing cytoskeleton (Fig. 3(*c*)).

Within this range, however, the model is currently unable to recreate the precise dependence of traction stress on aspect ratio that has been observed in past experiments [17,44]. This is likely due to the absence in the model of sarcomeric influence on cytoskeletal formation. Sarcomeres are the central contractile unit that make up the myofibrils [1,34] and their alignment and registration correlate with cell aspect ratio in the same way that traction stress changes with cell aspect ratio [38,51]. However, theoretical studies exploring force modulation via the sarcomeres have been difficult to produce because the alignment of sarcomeres depends on the location of the myofibril bundles. Future work in advancing this model will include incorporating sarcomeric registration into the developing network since it is now possible to visualize realistic cytoskeletal networks theoretically, allowing for the increasing-decreasing traction stress behavior to be captured.

Another possible reason for the difference between theoretical and experimental traction stress values may concern the way in which the cytoskeleton interacts with the nucleus. For our purposes, the nuclear cytoskeletal coupling was not explicitly explored and changes in nuclear shape during cytoskeletal network construction were not implemented. We proposed a simplistic interaction model where the nucleus was incorporated as an obstruction that the myofibril bundles tried to avoid during construction. However, the reality is much more complex as there is evidence that nuclear shape and cytoskeletal architecture are mechanically linked, likely via compressive loading [10,42]. Recent work has shed light on several nuclear envelope proteins such as nesprin that transmit forces from the cytoskeleton across the nuclear envelope [52]. A more granular nucleus-cytoskeleton interaction model may help remedy the traction stress discrepancy by physically linking the F-actin of the cytoskeleton to the nucleus through outer nuclear membrane proteins. Not only would this entanglement result in changes to the nuclear shape and predicted cytoskeletal architecture, but it could allow for force regulation throughout the cytoskeleton. Such regulation may influence the traction stress changes that occur during cell elongation. It would be beneficial to have time-lapse experimental data focusing on the feedback mechanism between the nucleus and cytoskeleton so that more granular interactions can be utilized in our model. Our baseline framework is setup to allow for these types of extensions theoretically and incorporating this information into the model is possible in the future once the experimental data is readily available.

In experimental cells subjected to the same environmental conditions, the overall cytoskeletal structure is largely consistent yet each cell exhibits variations in internal architecture [18]. While this phenomenon has been studied in individual cells using multiscale quantitative analysis [8], previous modeling attempts have been unable to reproduce networks that are structurally similar to experimental cells while also capturing cell-to-cell variability. Our approach produced individual myofibril bundles within the cell geometry, allowing for direct structural comparisons between model-generated networks and experiments. In all cases, a diverse array of meshworks were produced, due to the stochasticity built into the model equations, but the process of minimizing the cost associated with the developing mesh resulted in recurring structural properties. Of particular note is the presence of seemingly anomalous qualities in both model-generated and experimental cells (Figs. 4(*a*), 4(*b*)). By creating behavior consistent with global properties observed in the experimental cells as well as seemingly unique irregularities that may otherwise go un-noticed, the model brings the question of formation order and timing associated with internal structural components into the forefront.

In addition to being qualitatively similar to experimental cells, the simulations quantitatively recreated the multiscale relationship between structural consistency and cell aspect ratio (Figs. 4(*a*), 4(*b*)). When the model-generated networks were compared with the experimental cells, the results were consistently within the 95% confidence region produced by comparing experimental cells to each other (Figs. 4(*c*), 4(*d*)). Whereas previous models consistently yielded the same steady-state outcomes [13,14], our approach produced unique networks with each simulation, as is seen in the experimental cells.

5 Conclusion

The modeling framework outlined in this work provides a platform for future studies concerning the development of the cytoskeletal network and how it may be connected to cell contractility. A key achievement of our approach is the ability to recreate networks that demonstrate cell-to-cell variability using only basic cellular components. By modeling the feedback between focal adhesion maturation and cytoskeletal formation, it is possible to establish the exact placement of myofibril bundles for a specific cell. The ability to create and visualize individual myofibril curves within a two-dimensional geometry is an essential first step toward elucidating the influence of intracellular structures such as the nucleus on cellular organization and contractility. Since only a few processes were emphasized, there is potential for future model development by incorporating additional cellular components into the modeling framework. For instance, now that the location of a myofibril bundle can be determined, the sarcomeres that make up the bundle can be modeled and the influence of their registration can be analyzed. Thus, the model may be extended and used to explore how subcellular components like sarcomeres regulate cellular phenomena such as contractility. Our approach demonstrates that the cytoskeleton may form based on the unique subcellular interactions occurring within the specific cell. These interactions give rise to physical constraints that dictate which connections need to be established in order to create the most energetically beneficial and efficient cytoskeletal network.

The experimental data used here [8,38] avoided the possibility of multiple cells on a single ECM island by eliminating any island with more than two nuclei, which necessitated the exclusion of binucleated scenarios in our model considerations. As such, to compare model results with the data available, the scope of the current exploration was limited to cells with a single nucleus. Under our single-cell setup, we demonstrated that it's possible to build realistic cytoskeletal networks for various cell shapes. Now that the baseline modeling framework has been constructed where we can prescribe cell shape, size, and nucleus location, further explorations are possible. These could include more generalized setups such as single cells that are bi-nucleated, if bi-nucleated data becomes available. Our approach provides a foundation for these types of cases to be considered in the future by incorporating piecewise Bézier curves into the current modeling framework.

As recreated in our model, the relationship between the length of the myofibril and the resultant force generated at the adhesion site is more complicated than a simple force-length dependency. Not only should the number of myofibrils created to be considered, but the resulting sarcomeric structure may also play a crucial role. Indeed, it is possible to estimate the contractile forces at the adhesion sites for a given myofibril but how those forces propagate along the myofibril and what role they play in the eventual sarcomeric pattern that is formed has yet to be fully realized. While it may be possible to recreate the observed sarcomeric pattern using force estimates at the endpoints for a single myofibril, generalizing the sarcomeric pattern-creation to multiple interacting myofibrils with curvature in a multidimensional space where the adhesion sites are not necessarily in line with each other is more challenging. We believe our model provides a critical step toward addressing this future problem by being able to reliably recreate the two important factors needed to tackle the sarcomeric pattern-formation problem: a realistic internal architecture that varies with cell geometry and explicit traction force values that allow for direct comparison with both experimental and model-generated data.

Funding Data

- National Institutes of Health (Grant No. HL 116270; Funder ID: 10.13039/100000002).
- National Science Foundation (Grant No. DMS1763272; Funder ID: 10.13039/100000001).
- Simons Foundation (Grant No. 594598 QN; Funder ID: 10.13039/100000893).

References

[1] Sheehy, S. P., Grosberg, A., and Parker, K. K., 2012, "The Contribution of Cellular Mechanotransduction to Cardiomyocyte Form and Function," Biomech. Model. Mechanobiol., **11**(8), pp. 1227–1239.
[2] Ehler, E., 2016, "Cardiac Cytoarchitecture - Why the "Hardware" is Important for Heart Function!," Biochim. et Biophysica Acta, **1863**(7), pp. 1857–1863.
[3] Liang, J., Huang, B., Yuan, G., Chen, Y., Liang, F., Zeng, H., Zheng, S., Cao, L., Geng, D., and Zhou, S., 2017, "Stretch-Activated Channel Piezo1 is Up-Regulated in Failure Heart and Cardiomyocyte Stimulated by AngII," Am. J. Transl. Res., **9**(6), pp. 2945–2955.
[4] Core, J. Q., Mehrabi, M., Robinson, Z. R., Ochs, A. R., McCarthy, L. A., Zaragoza, M. V., and Grosberg, A., 2017, "Age of Heart Disease Presentation and Dysmorphic Nuclei in Patients With LMNA Mutations," PloS One, **12**(11), p. e0188256.
[5] Golob, M., Moss, R. L., and Chesler, N. C., 2014, "Cardiac Tissue Structure, Properties, and Performance: A Materials Science Perspective," Ann. Biomed. Eng., **42**(10), pp. 2003–2013.
[6] Sequeira, V., Nijenkamp, L. L. A. M., Regan, J. A., and van der Velden, J., 2014, "The Physiological Role of Cardiac Cytoskeleton and Its Alterations in Heart Failure," Biochim Biophys Acta, **1838**(2), pp. 700–722.
[7] Gerdes, A. M., Kellerman, S. E., Moore, J. A., Muffly, K. E., Clark, L. C., Reaves, P. Y., Malec, K. B., McKeown, P. P., and Schocken, D. D., 1992, "Structural Re-Modeling of Cardiac Myocytes in Patients With Ischemic Cardiomyopathy," Circulation, **86**(2), pp. 426–430.
[8] Drew, N. K., Johnsen, N. E., Core, J. Q., and Grosberg, A., 2016, "Multiscale Characterization of Engineered Cardiac Tissue Architecture," ASME J. Biomech. Eng., **138**(11), p. 111003.
[9] Bathe, M., Heussinger, C., Claessens, M. M. A. E., Bausch, A. R., and Frey, E., 2008, "Cytoskeletal Bundle Mechanics," Biophys. J., **94**(8), pp. 2955–2964.
[10] Vishavkarma, R., Raghavan, S., Kuyyamudi, C., Majumder, A., Dhawan, J., and Pullarkat, P. A., 2014, "Role of Actin Filaments in Correlating Nuclear Shape and Cell Spreading," Plos One, **9**(9), p. e107895.
[11] Sherman, W. F., and Grosberg, A., 2020, "Exploring Cardiac Form and Function: A Length-Scale Computational Biology Approach," WIREs Syst. Biol. Med., **12**(2), p. e1470.
[12] Kassianidou, E., Brand, C. A., Schwarz, U. S., and Kumar, S., 2017, "Geometry and Network Connectivity Govern the Mechanics of Stress Fibers," Proc. Nat. Acad. Sci., **114**(10), pp. 2622–2627.
[13] Yuan, H., Marzban, B., and Parker, K. K., 2017, "Myofibrils in Cardiomyocytes Tend to Assemble Along the Maximal Principle Stress Directions," ASME J. Biomech. Eng., **139**(12), p. 121010.
[14] Grosberg, A., Kuo, P.-L., Guo, C.-L., Geisse, N. A., Bray, M.-A., Adams, W. J., Sheehy, S. P., and Parker, K. K., 2011, "Self-Organization of Muscle Cell Structure and Function," PLOS Comput. Biol., **7**(2), p. e1001088.
[15] Oakes, P. W., Banerjee, S., Marchetti, M. C., and Gardel, M. L., 2014, "Geometry Regulates Traction Stresses in Adherent Cells," Biophys. J., **107**(4), pp. 825–833.
[16] Novak, I. L., Slepchenko, B. M., Mogilner, A., and Loew, L. M., 2004, "Cooperativity Between Cell Contractility and Adhesion," Phys. Rev. Lett., **93**(26), p. 268109.
[17] Kuo, P.-L., Lee, H., Bray, M.-A., Geisse, N. A., Huang, Y.-T., Adams, W. J., Sheehy, S. P., and Parker, K. K., 2012, "Myocyte Shape Regulates Lateral Registry of Sarcomeres and Contractility," Am. J. Pathol., **181**(6), pp. 2030–2037.
[18] Parker, K. K., Tan, J., Chen, C. S., and Tung, L., 2008, "Myofibrillar Architecture in Engineered Cardiac Myocytes," Circulation Res., **103**(4), pp. 340–342.
[19] Balaban, N. Q., Schwarz, U. S., Riveline, D., Goichberg, P., Tzur, G., Sabanay, I., Mahalu, D., Safran, S., Bershadsky, A., Addadi, L., and Geiger, B., 2001, "Force and Focal Adhesion Assembly: A Close Relationship Studied Using Elastic Micropatterned Substrates," Nat. Cell Biol., **3**(5), pp. 466–472.
[20] Livne, A., and Geiger, B., 2016, "The Inner Workings of Stress Fibers - From Contractile Machinery to Focal Adhesions and Back," J. Cell Sci., **129**(7), pp. 1293–1304.
[21] Wu, C., 2007, "Focal Adhesion: A Focal Point in Current Cell Biology and Molecular Medicine," Cell Adhes. Migr., **1**(1), pp. 13–18.
[22] Schwarz, U. S., Erdmann, T., and Bischofs, I. B., 2006, "Focal Adhesions as Mechanosensors: The Two-Spring Model," Biosystems, **83**(2–3), pp. 225–232.
[23] Welf, E. S., Naik, U. P., and Ogunnaike, B. A., 2012, "A Spatial Model for Integrin Clustering as a Result of Feedback Between Integrin Activation and Integrin Binding," Biophys. J., **103**(6), pp. 1379–1389.
[24] Liu, Y., Medda, R., Liu, Z., Galior, K., Yehl, K., Spatz, J. P., Cavalcanti-Adam, E. A., and Salaita, K., 2014, "Nanoparticle Tension Probes Patterned at the Nanoscale: Impact of Integrin Clustering on Force Transmission," Nano Lett., **14**(10), pp. 5539–5546.
[25] Roca-Cusachs, P., Gauthier, N. C., Rio, A. D., and Sheetz, M. P., 2009, "Clustering of Alpha(5)Beta(1) Integrins Determines Adhesion Strength Whereas Alpha(v)Beta(3) and Talin Enable Mechanotransduction," Proc. Natl. Acad. Sci. USA, **106**(38), pp. 16245–16250.
[26] Falzone, T. T., Lenz, M., Kovar, D. R., and Gardel, M. L., 2012, "Assembly Kinetics Determine the Architecture of Alpha-Actinin Crosslinked f-Actin Networks," Nat. Commun., **3**(1), p. 861.
[27] Tan, J. L., Tien, J., Pirone, D. M., Gray, D. S., Bhadriraju, K., and Chen, C. S., 2003, "Cells Lying on a Bed of Microneedles: An Approach to Isolate Mechanical Force," PNAS, **100**(4), pp. 1484–1489.
[28] Duncan, J. S., Lee, F. A., Smeulders, A. W. M., and Zaret, B. L., 1991, "A Bending Energy Model for Measurement of Cardiac Shape Deformity," IEEE Trans. Med. Imaging, **10**(3), pp. 307–320.
[29] Veltkamp, R. C., and Wesselink, W., 1995, "Modeling 3D Curves of Minimal Energy," Comput. Graph. Forum, **14**(3), pp. 97–110.
[30] Hale Eriskin, H., and Yu ̈Cesan, A., 2016, "Bézier Curve With a Minimal Jerk Energy," Math. Sci. Appl. E-Notes, **4**(10), pp. 139–148.
[31] Benoit, S., 2010, "A Minimum-Energy Quadratic Curve Through Three Points and Corresponding Cubic Hermite Spline," arXiv: Numerical Analysis.
[32] Ursell, T., Kondev, J., Reeves, D., Wiggins, P. A., and RobPhillips, R., 2008, *Mechanosensitive Ion Channels*, **1**, Springer, Dordrecht, Chap. Role of Lipid Bilayer Mechanics in Mechanosensation, pp. 37–70.
[33] Soukhovolsky, V. G., Ivanova, Y. D., Shulman, K., Mazharov, V. F., Tarasova, I. V., Tarasova, O. V., and Khlebopros, R. G., 2015, "The Population Dynamics of Cancer Incidence: The Model of a Second-Order Phase Transition," Biophysics, **60**(4), pp. 639–646.
[34] Sanger, J. W., Kang, S., Siebrands, C. C., Freeman, N., Du, A., Wang, J., Stout, A. L., and Sanger, J. M., 2006, "How to Build a Myofibril," J. Muscle Res. Cell Motility, **26**(6–8), pp. 343–354.
[35] Sanger, J. M., Mittal, B., Pochapin, M. B., and Sanger, J. W., 1986, "Myofibrillogenesis in Living Cells Microinjected With Fluorescently Labeled Alpha-Actinin," J. Cell Biol., **102**(6), pp. 2053–2066.
[36] Drew, N. K., Eagleson, M. A., Baldo, Jr., D. B., Parker, K. K., and Grosberg, A., 2015, "Metrics for Assessing Cytoskeletal Orientational Correlations and Consistency," PLOS Comput. Biol., **11**(4), p. e1004190.
[37] Knight, M. B., Drew, N. K., McCarthy, L. A., and Grosberg, A., 2016, "Emergent Global Contractile Force in Cardiac Tissues," Biophys. J., **110**(7), pp. 1615–1624.
[38] Morris, T. A., Naik, J., Fibben, K. S., Kong, X., Kiyono, T., Yokomori, K., and Grosberg, A., 2020, "Striated Myocyte Structural Integrity: Automated Analysis of Sarcomeric z-Discs," PLOS Comput. Biol., **16**(3), p. e1007676.
[39] Wozniak, M. A., Modzelewska, K., Kwong, L., and Keely, P. J., 2004, "Focal Adhesion Regulation of Cell Behavior," Biochim Biophys Acta, **1692**(2–3), pp. 103–119.
[40] Alberts, B., Johnson, A., Lewis, J., Raff, M., Roberts, K., and Walter, P., 2002, *Molecular Biology of the Cell*, 4th ed., Garland Science, New York, Chap. Integrins.
[41] Fruleux, A., and Hawkins, R. J., 2016, "Physical Role for the Nucleus in Cell Migration," J. Phys.: Condens. Matter, **28**(36), p. 363002.
[42] Versaevel, M., Grevesse, T., and Gabriele, S., 2012, "Spatial Coordination Between Cell and Nuclear Shape Within Micropatterned Endothelial Cells," Nat. Commun., **3**(1), p. 671.
[43] Choi, J., Curry, R., and Elkaim, G., 2008, "Path Planning Based on Bézier Curve for Autonomous Ground Vehicles," Advances in Electrical and Electronics Engineering - IAENG Special Edition of the World Congress on Engineering and Computer Science, San Francisco, CA, Oct. 22–24, pp. 158–166.
[44] Ribeiro, A. J. S., Ang, Y.-S., Fu, J.-D., Rivas, R. N., Mohamed, T. M. A., Higgs, G. C., Srivastava, D., and Pruitt, B. L., 2015, "Contractility of Single Cardiomyocytes Differentiated From Pluripotent Stem Cells Depends on Physiological Shape and Substrate Stiffness," Proc. Natl. Acad. Sci., **112**(41), pp. 12705–12710.
[45] McCain, M. L., Yuan, H., Pasqualini, F. S., Campbell, P. H., and Parker, K. K., 2014, "Matrix Elasticity Regulates the Optimal Cardiac Myocyte Shape for Contractility," Am. J. Physiol. Heart Circ. Physiol., **306**(11), pp. H1525–H1539.
[46] Davis, J., Davis, L. C., Correll, R. N., Makarewich, C. A., Schwanekamp, J. A., Moussavi-Harami, F., Wang, D., York, A. J., Wu, H., Houser, S. R., Seidman, C. E., Seidman, J. G., Regnier, M., Metzger, J., Wu, J. C., and Molkentin, J. D., 2016, "A Tension-Based Model Distinguishes Hypertrophic Versus Dilated Cardiomyopathy," Cell, **165**(5), pp. 1147–1159.
[47] Edelstein-Keshet, L., 1998, "A Mathematical Approach to Cytoskeletal Assembly," Eur. Biophys. J., **27**(5), pp. 521–531.
[48] Borau, C., Kamm, R. D., and Garćıa-Aznar, J. M., 2014, "A Time-Dependent Phenomenological Model for Cell Mechanosensing," Biomech. Model. Mechanobiol., **13**(2), pp. 451–462.
[49] Nicolas, A., Besser, A., and Safran, S. A., 2008, "Dynamics of Cellular Focal Adhesions on Deformable Substrates: Consequences for Cell Force Microscopy," Biophys. J., **95**(2), pp. 527–539.
[50] Deshpande, V. S., McMeeking, R. M., and Evans, A. G., 2006, "A Bio-Chemo-Mechanical Model for Cell Contractility," Proc. Natl. Acad. Sci., **103**(38), pp. 14015–14020.
[51] Dasbiswas, K., Majkut, S., Discher, D. E., and Safran, S. A., 2015, "Substrate Stiffness-Modulated Registry Phase Correlations in Cardiomyocytes Map Structural Order to Coherent Beating," Nat. Commun., **6**(1), p. 6085.
[52] Lammerding, J., 2011, "Mechanics of the Nucleus," Compr. Physiol., **4**(1), pp. I13–I17.